ATLAS Internal Note
MUON-NO-055
12 September 1994

BROOKHAVEN NATIONAL LABORATORY

September 10, 1994 BNL-CSC-94-2

Position and Timing Resolution of Interpolating Cathode Strip Chambers in a Test Beam

V. Gratchev[a,1] O. Kiselev[a,1], S. McCorkle[a], M. Mohammadi[b], P. O'Connor[a], V. Polychronakos[a], O. Prokofiev[a,1], V. Radeka[a], J. Shank[c], G. Smith[a], J. Sondericker III[a], D. Stephani[a], V. Tcherniatine[a,2], A. Vanyashin[a,b,2], S. Whitaker[c], B. Yu[a]

[a] *Brookhaven National Laboratory, Upton NY 11973, USA*
[b] *State University of New York at Stony Brook, Physics Department, Stony Brook NY 11794, USA*
[c] *Boston University, Physics Department, Boston MA 02215, USA*

Abstract

Design and construction details are presented of a four-layer, position sensitive, cathode strip chamber and a low cost, highly multiplexed readout system based on monolithic circuit technology that are well suited for a muon detector at future hadron colliders. Track location is determined by interpolation of the cathode induced charge, using a new design with intermediate strips between readout nodes to reduce the number of channels and improve position resolution and linearity. Results are reported from tests with an ^{55}Fe source and a 300 GeV/c muon beam in RD5 at CERN. The beam test demonstrated position resolution of 40 μm per layer which is less than 1% of the readout pitch. The timing resolution for the entire four-layer detector was 3.6 ns r.m.s. which is adequate for fully efficient beam crossing identification in an LHC experiment.

to be submitted to Nuclear Instruments and Methods

[1] Visitor from St.Petersburg Nuclear Physics Institute, Gatchina, Russia
[2] Visitor from Moscow Engineering Physics Institute, Moscow, Russia

1 Introduction

The high precision position measurement obtainable with Cathode Strip Chambers (CSC) has been demonstrated in [1]–[10]. The widespread use of this technique was limited by the large channel count of analog electronics required to provide induced charge measurement on each strip with a 1% precision. This factor is no longer that limiting due to recent developments in multiplexed analog electronics and high speed signal digitization [11]. The CSC technology has a number of advantages over drift chamber technology. The two most important are the ease of achieving performance stability and the inherent mechanical precision. CSC performance stability is determined by the stability of the readout electronics. The latter is much easier to provide via calibration, than is, *e.g.*, the drift velocity stability required for good drift chamber performance. The high mechanical precision is easily achieved because the position sensing cathode strips are produced lithographically. Those two benefits are essential for the large muon systems of future collider experiments.

This paper presents beam test results for the interpolating CSC prototype, which has been developed in the framework of the R&D program for the GEM detector muon system [12]. All results presented are obtained with the low cost highly multiplexed readout system based on an existing custom integrated circuit.

2 Cathode Strip Chamber

2.1 CSC Design

One of the prototyping goals was to test the materials suitable for the full scale CSCs for the muon system for future hadron colliders. The CSC design shown in Figure 1 uses low mass construction. The detector was built as two two-layer modules. The two layers are formed by three flat, rigid panels, each made of a 23 mm thick sheet of nomex honeycomb (hexcel) and two 1.19 mm thick copper-clad FR4 laminates (Figure 1b.), the 17 μm thick copper forms the cathodes. The panel frames are made of machined zelux (fiberglass reinforced lexan). They provide the 2.54 mm step for the anode plane of gold-plated tungsten wires 30 μm in diameter. The frames of the outer panels have a milled cavity with enough room for the

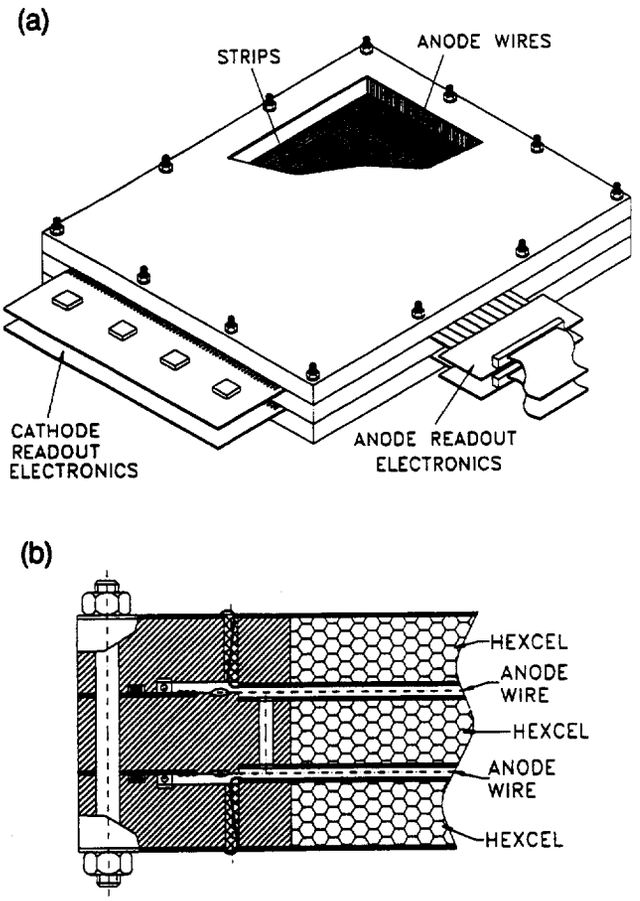

Figure 1: A two-layer module of the Cathode Strip Chamber.

epoxy beads for the wire attachment as well as the anode blocking capacitors. A rubber gasket just outside this cavity provides the gas seal for the assembly. In this manner no components under high voltage are outside the seal thus minimizing the risk of high voltage breakdowns. The sensitive area of this prototype is 45×36 cm^2.

The position sensing cathode strips are lithographically etched on either side of the central panel[1]. These cathodes are precisely positioned with respect to each other with the aid of locating pins. The strips are oriented at 90° with respect to the anode wires, providing the precision position measurement in the direction along the anode wires. The outer cathodes in each layer are continuous (un-etched) copper planes.

On one of the continuous cathodes, four windows of approximately 4×3 cm^2 were cut out. Four collimators made of 0.63 mm half hard brass shim stock were placed in these windows. Each collimator has 25 precision slits 100 μm wide, 1.5 cm long cut every 1/5 of the readout pitch. A thin layer of mylar glued on the back side of the collimators guarantees the integrity of the gas volume. Corresponding windows were opened on the outside skin of this panel to allow penetration of the soft X-rays from an ^{55}Fe source.

The CSCs are Multiwire Proportional Chambers with a symmetric cell in which the anode-cathode spacing, d, is equal to the wire pitch, S, which equals 2.54 mm (Fig. 2). The readout pitch, W, is 5.08 mm. (This is true for 3/4 of the area of the chambers. For the remaining the pitch was increased to 7.00 mm.) Thus the ratio of the readout pitch to anode-cathode spacing is $W/d = 2$. Without the intermediate strips such a high ratio would result in significant (>50%) position encoding differential non-linearity since the FWHM of the cathode induced charge is about 1.5d. It has been shown [13] that the condition for a minimal (≈1%) differential non-linearity is $W/d \leq 0.8$. This condition would dictate a readout pitch of 2 mm resulting in an unacceptably large number of channels. The linearity of response can be restored to near optimum with the use of intermediate strips between readout nodes which provide increased charge sampling frequency and are capacitively coupled to the adjacent readout strips [14], [15].

[1]For the large 2.5 × 1 m industrially produced panel the precision of the cathode strips etched by this technique was measured to be $\sigma \leq 15\mu$m

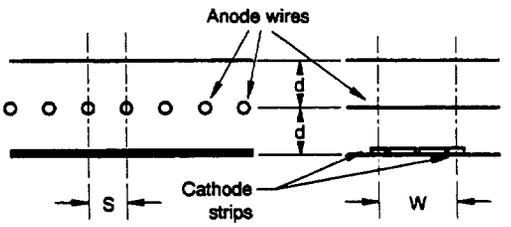

Figure 2: Schematic diagram of the Cathode Strip Chamber. In our chamber the anode-cathode spacing, d = 2.54 mm, wire pitch, S = 2.54 mm, the readout pitch, W = 5.08 mm.

We used an arrangement with two intermediate strips which is shown in Figure 3 along with the equivalent electrical circuit. For optimal capacitive interpolation, the interstrip capacitance, C_1, must be much larger than that of a strip to ground, C_2, ($C_1/C_2 \geq 10$). For the present design of the CSCs, $C_1/C_2 \approx$ 10–12. Further optimization results in intermediate strips of a slightly larger width than the readout strips [16]. For this prototype, the gap between strips is 0.25 mm, the readout strip width is 1.07 mm and that of the two intermediate strips 1.63 mm (Fig. 3a). It is necessary to provide a high resistance path to ground to maintain the intermediate strips at the proper DC potential. A thin strip of resistive epoxy (conductivity 6 MΩ per square) was silk screened on the tips of the strips at the end of the cathode opposite to the amplifiers.

2.2 Gas Amplification and Gain Uniformity

Gas gain uniformity across the active area of the detector is an important chamber property characterizing chamber performance stability. For studies of the gain uniformity we used the 60 keV X-rays from an ^{241}Am source. This source was used because of the high penetrating power of the X-rays. Such energetic X-rays, however, produce ionization with a wide amplitude spectrum making quantitative measurements difficult. A benefit of using copper cathodes is the 8 keV Cu fluorescence line quite distinctly visible in our chambers. Using this peak in the ^{241}Am spectrum we were able to measure the gas gain in the entire chamber area. All gain values are contained within ±20%

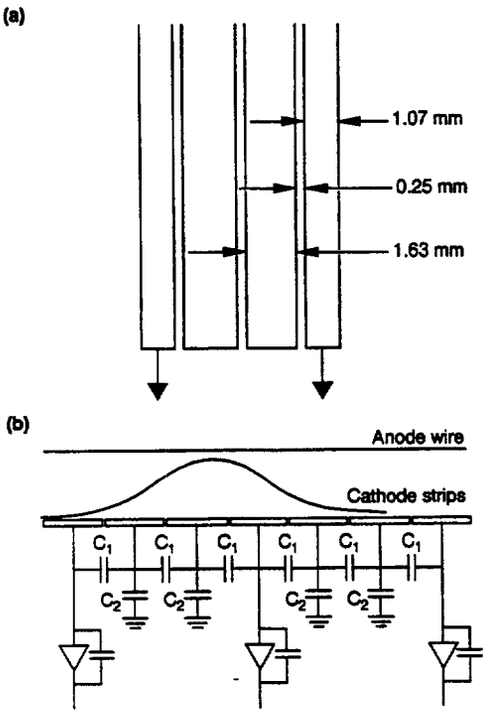

Figure 3: (a) The optimized widths of the readout and intermediate strips. (b) The equivalent circuit showing the principle of capacitive interpolation using the two intermediate strips.

indicating that the cathode peak to peak variation from the perfect flatness was not more than ≈ 75 μm.

The absolute gas gain was measured using the ^{55}Fe source illuminating the chamber through one of the four collimators. Both the cathode strips and the anode wires were used in independent measurements. In order to measure the anode charge a QVT was attached to the output of one of the wire channels. To obtain the total charge from the cathodes, the node with the largest pulse height and the amplitudes of its four nearest neighbors were added. Consistent results were obtained with both methods. In both cases the fraction of the charge collected was taken into account in order to estimate the true gain.

2.3 Operating Gas

There are three basic requirements that need to be met by a chamber gas suitable for a CSC-based muon detectors at future hadron colliders. These are:

- High drift velocity (> 60 μm/ns)
- Low ($< 10°$) Lorentz angle
- Non-flammable

Such a gas has been identified and used in our tests. The composition of the gas is 30%Ar+50%CO_2+20%CF_4. Drift velocity and Lorentz angle dependence on electric and magnetic fields for this mixture are shown in Figure 4 [17]. To study the CF_4 presence effects we also have done some measurements with a 80%Ar+20%CO_2 gas mixture.

2.4 Electronic Readout

2.4.1 Cathode Strip Readout

The ultimate position resolution of the CSCs depends on physical processes in the gas. However, electronic noise can degrade the resolution if the overall signal-to-noise ratio becomes too low. Note that one can not arbitrarily increase the gas amplification in order to compensate for poor noise performance. It has been shown [18] that for most gases the resolution degrades for anode charge larger than $\approx$2 pC due, primarily, to photon mediated avalanche fluctuations.

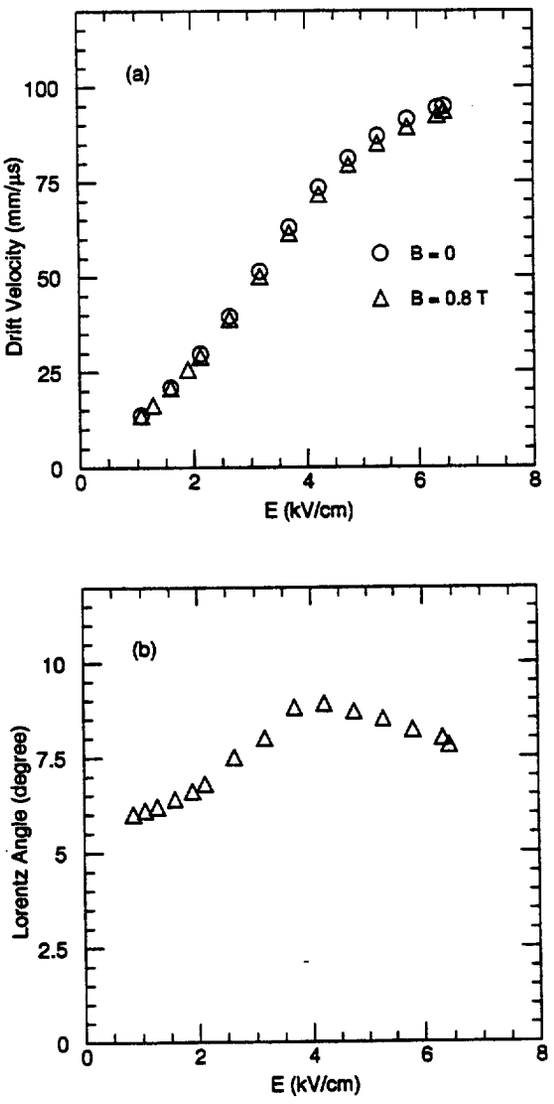

Figure 4: The 30%Ar+50%CO_2+20%CF_4 gas mixture properties. (a) The drift velocity dependence on the electric field with and without magnetic field. (b) Lorentz angle dependence on the electric field at $B = 0.8$ T.

We have designed a readout system (Figure 5) which features a 16-channel monolithic shaping amplifier with multiplexed output. This CMOS integrated circuit (AMPLEX) was designed at CERN for use with silicon detectors with less than 10 pF capacitance [11]. Hence, the slope of the equivalent noise charge as a function of input capacitance is high (> 35 electrons/pF, depending on amplifier bias current). To obtain adequate noise performance with CSCs we introduced a low noise, high performance, hybrid charge sensitive preamplifier in front of each AMPLEX channel. Each preamplifier in a three channel hybrid circuit has a JFET front end (Interfet NJ132L) optimized for an input electrode capacitance range of 50 – 150 pF corresponding to cathode strip lengths of 1 – 3 m. The feedback capacitor C_f is 5 pF and the feedback resistor is 50 MΩ so that it contributes negligible parallel noise even for long shaping times. The hybrid preamplifier is coupled to the AMPLEX by a 1.35 pF capacitor (C_c), which allows the AMPLEX amplifier to operate with an effective input capacitive load of only 1.35 pF, close to its optimum. A single transistor inverter matches the polarities of the two amplifiers and provides an additional gain of 3–4 to compensate for the gain loss due to C_c/C_f.

Although the monolithic AMPLEX still dominates the electronic noise, the noise slope as a function of input capacitance is now determined by the hybrid and is only 7 electrons/pF for the shaping time of 550 ns.

The multiplexed outputs from all AMPLEX chips are buffered and sent to an on-board unity gain buffer. A total of 4096 channels may be read by a single CAMAC module which digitizes the analog signals with a 10-bit flash ADC and stores the information in a memory [19]. It results in a compact, low cost readout system with a small number of cables. This immensely facilitates the task of shielding the modules against electromagnetic interference as well as controlling ground loops, the bane of precision measurements in large systems.

2.4.2 Calibration of the Cathode Readout System

Knowledge of the relative electronic gains in neighboring channels at the ≤1% level is necessary to achieve good position resolution of ≤ 50 μm.

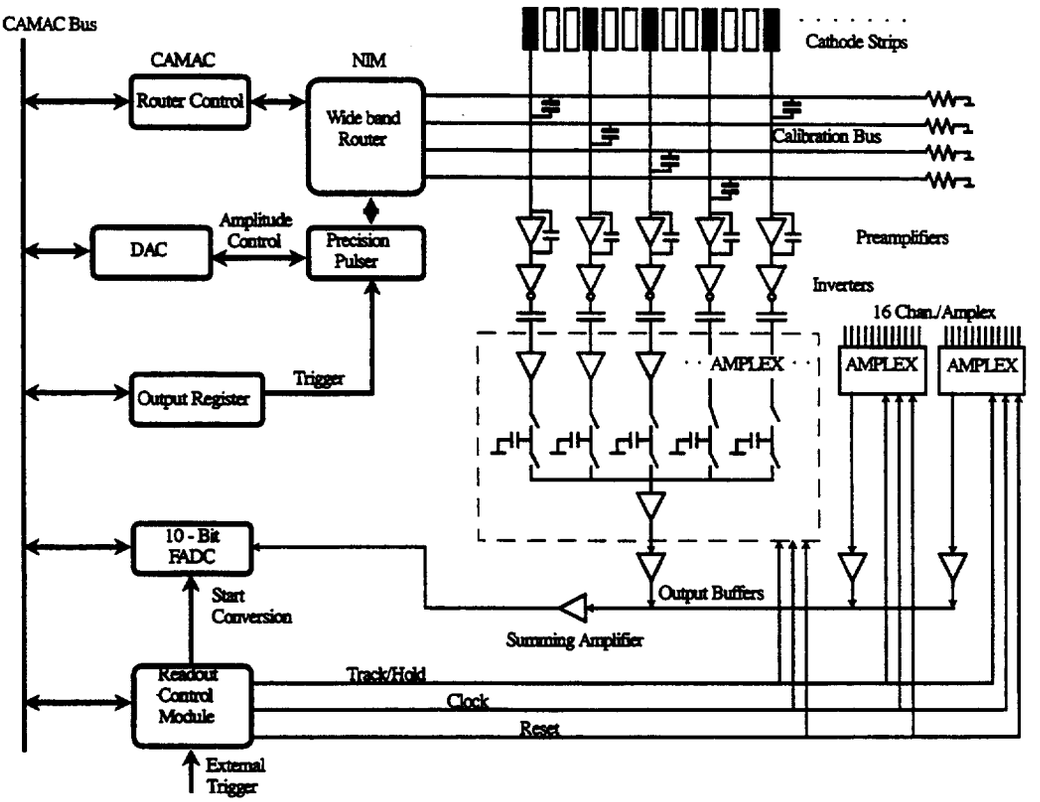

Figure 5: Block diagram of the cathode readout.

Precision calibration capacitors of 0.7 pf were built into the multilayer readout printed circuit board. Every fourth capacitor was connected to the same calibration line which was terminated into 50 Ω. The resulting four calibration lines were fed by the same precision pulser, one at a time via a computer controlled wide-band router. The amplitude of the precision pulser as well as its trigger were also computer controlled. At regular intervals, approximately daily, calibration data were taken by stepping the pulser amplitude through 30 values spanning the whole dynamic range in use. A few hundred events were accumulated for every pulser value and the mean values and r.m.s. deviations calculated for all channels. A polynomial was then fit to these values. This was necessary because, in order to achieve as much dynamic range as possible, we used the AMPLEX chip in a region well beyond its linear range. The fit coefficients were then used in the data analysis in order to calculate the induced charge. Figure 6a shows a typical calibration curve. In order to check this calibration procedure a known pulse was injected in all channels. The difference between expected and measured charge is shown in Figure 6b demonstrating the calibration accuracy better than 0.1% just after the calibration. The accuracy slightly degraded one day after the calibration (Fig. 6b). To account for differences in calibration capacitances and channel to channel cross-talk during the common calibration procedure described above, corrections were measured for each channel by comparing the common and the individual calibration. The individual calibration was done using the same capacitor for each channel and the calibration signal was applied to one channel at a time. The application of these two calibration procedures to determine the actual charge on each cathode strip is discussed in Section 5, below.

The AMPLEX integrated circuit utilizes a track-and-hold technique to measure signal amplitude: all 16 input channels are held, then sequentially multiplexed onto the output line. The track-and-hold timing is very important for a precision charge measurement. If the delays used for the track-and-hold signals in calibration and in a particle trigger are different, the channel-to-channel variations in shaping time would degrade the charge measurement precision. The dependence of the calibration error on the time differ-

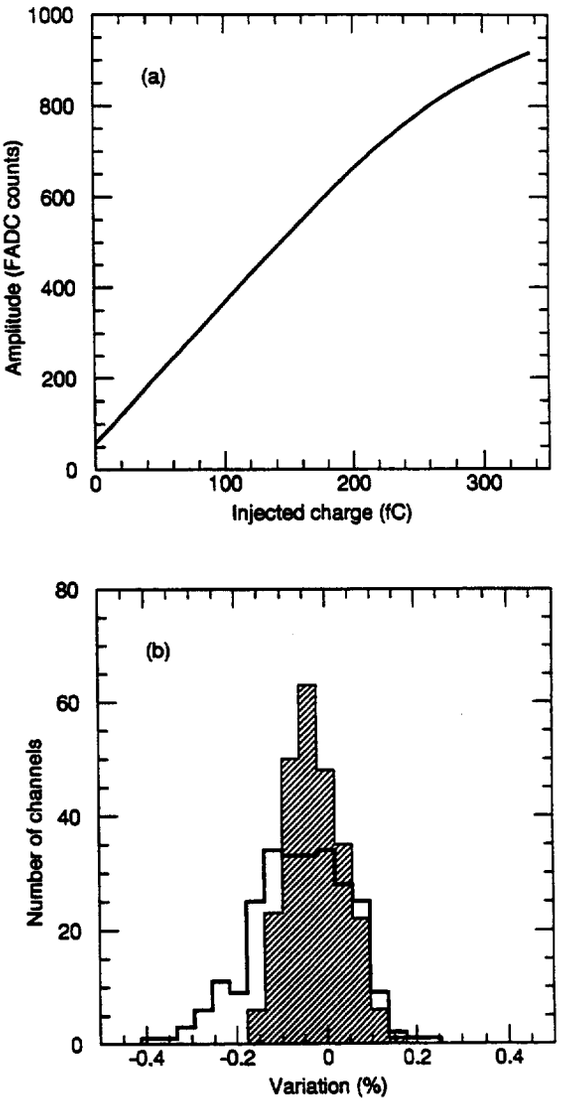

Figure 6: (a) A typical calibration curve. (b) The difference between expected and measured charge just after the calibration (shaded histogram) and one day after the calibration (open histogram).

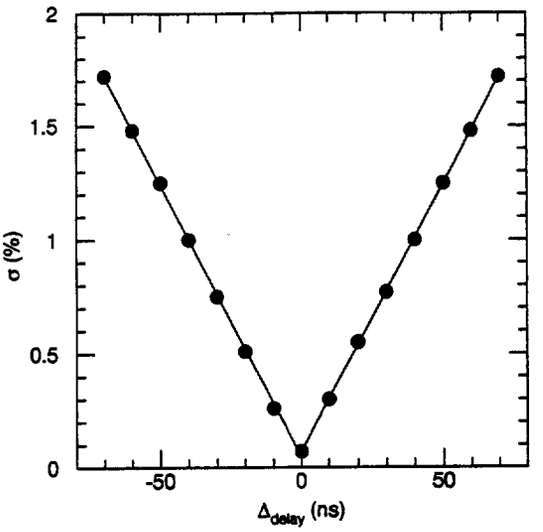

Figure 7: The dependence of the calibration error on the difference of track-and-hold arrival times during calibration and running, Δ_{delay}.

ence is shown in Figure 7. The calibration error is determined as the r.m.s. of the variation distribution (Fig. 6b). The calibration error is minimal when the track-and-hold delays for calibration and for particle trigger are equal ($\Delta_{delay} = 0$). To limit calibration errors below 0.5% the difference in delays should be within ±20 ns.

2.4.3 Anode Readout

The anode readout is less demanding in spite of the fact that fast shaping is required (30 ns) in order to provide trigger information and bunch crossing tagging. The anode wires were connected in groups of 20 providing 5 cm wide hodoscope elements. We used a bipolar, grounded-base amplifier (BNL Instrumentation Division, IO-354-2) and a 30 ns shaping amplifier (BNL Instrumentation Division, IO-638-01). These are implemented in thin film hybrid technology and are mounted on a printed circuit board on the detector. They are followed by on-board discriminators which provide a fast OR for self-triggering. Thus the chamber is self-sufficient, not requiring any additional detectors in order to be tested with sources, cosmic rays, or particle beams. The discriminator outputs were used for input into TDCs to obtain additional information during the beam test.

3 Monte Carlo Simulations

To optimize chamber performance and study the position resolution dependence on different factors, we developed a chamber simulation program that takes into account the following processes:

- Cluster production. (Position and size of primary ionization clusters along the particle track).
- Diffusion.
- δ-electron range.
- Lorentz angle effect.
- Chamber geometry effects.
- Charge multiplication.
- Induced charge distribution on cathode.
- Anode screening effect. (The dependence of induced charge on avalanche location w.r.t. the segmented cathode.)
- Readout electronics noise.
- Calibration uncertainties. (They include all uncertainties due to the calibration procedure, cross-talk and tails correction.)

The cluster position along the particle track was simulated according to a Poisson distribution. The particle energy loss in the gas was simulated using a method from [20], that takes into account detector media atomic levels based on photoabsorbtion cross-sections. Based on this energy loss, the number of electrons in a cluster were simulated according to a binomial distribution [21]. For each electron produced, a process of multiplication in a strong electric field near the anode was simulated according to a Polya distribution [22]. To obtain the cathode induced charge distribution, a one-parameter Gatti function was used [23]. The same strip geometry as in the real chamber — two adjacent interpolating strips for each readout strip — was used in simulation. Electronic noise and calibration uncertainties were simulated according to Gaussian distributions. Noise contribution was added to a strip charge, which was then multiplied by a calibration uncertainty. The value of electronic noise used was the same as in real data taking.

The Monte Carlo results and comparison with the data are described below in Section 6.

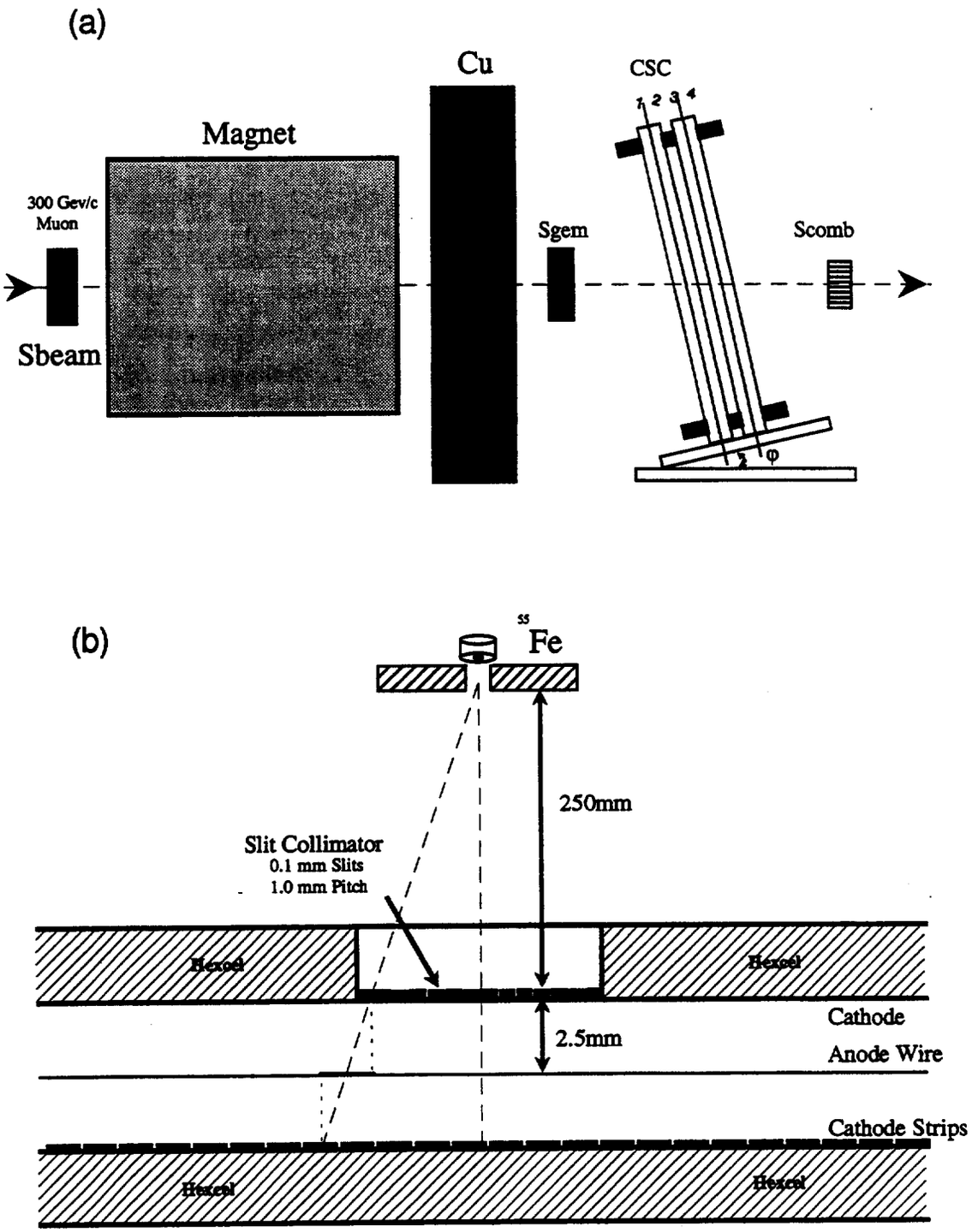

Figure 8: (a) The CSC setup during the beam test. (b) The CSC setup during ^{55}Fe measurements.

4 Test setup

During September 1993, the CSC was tested at the RD5 beam at CERN [24]. Figure 8a shows the CSC setup during the test. Most of the runs used a 300 GeV/c muon beam. Beam divergence due to multiple scattering (in the RD5 magnet) at this momentum was limited to 2 mrad. The illuminated area of the chamber was determined by the RD5 trigger counters. Some dedicated runs have a comb counter in the trigger. The comb counter consists of alternate layers of 1.0 mm plastic and 0.1 mm scintillator (Fig. 8a). When this counter was included in the trigger, only particles coming through the scintillator were selected. Thus, one is selecting from the beam slices of 0.1 mm width with a known 1.1 mm pitch. These data provide the absolute spatial scale and were used to check the measured position nonlinearity inherent in any position determination algorithm based on charge distribution in adjacent strips. A micrometer mount enabled a precision shift of the comb counter position to scan for nonlinearity with fine steps. The CSC was installed on a rotating table, allowing θ angle variation. Anode wires were vertical and cathode strips were horizontal. The φ angle was changed by tilting the table. The upstream magnet was used to scan the beam over the chamber, for a global position resolution study. The readout shown schematically in Figure 5 was incorporated in the RD5 Data Acquisition System.

The test setup during the ^{55}Fe X-ray measurements is shown on Figure 8b. X-rays reached the CSC through a precision slit collimator and thus have known position and spread. This is needed for position nonlinearity studies. For the X-ray measurements a stand-alone Macintosh based DAQ system was used.

5 Data Analysis

5.1 Charge Measurement

As we mentioned above the CSCs position resolution is directly related to the accuracy of the cathode strip induced charge measurement. The actual charge of each strip was determined from the measured Flash ADC (FADC) value using the following procedure:

i) Pedestal Subtraction. Pedestal values for each readout channel were determined from the most recent calibration run. Empty events in every run were used to determine a pedestal shift, common to all channels, since the calibration. (Due to the large angle scatter of triggered muons about 5% of events were empty in most runs.) Channel-to-channel pedestal variations since calibration were small and not taken into account.

Pedestal subtracted FADC values were obtained by subtracting the pedestals obtained from calibration and corrected for the common pedestal shift.

ii) Calibration. During the run, the channel calibration (described in Section 2.4.2) was done once a day. We refer to that as the common calibration. The common calibration is easy to implement and it takes less time to calibrate all the channels since one fourth of the channels are calibrated simultaneously. But it suffers from some drawbacks, *e.g.*, the calibration capacitors used have a ($\approx$ 1%) variation, affecting the charge measurement accuracy. To account for these, we measured differences between the common and the individual calibration — a more tedious procedure where only one channel is calibrated at a time and the same capacitor is used to calibrate all channels.

A strip charge was obtained from the pedestal subtracted FADC value by applying the common calibration polynomial, then correcting this result using the measured individual-common calibration differences.

iii) Cross-Talk Correction. There is a cross-talk between AMPLEX channels — the signal in one channel induces a $\approx$ 1.5% signal of opposite polarity in all other channels of the same AMPLEX [11]. To achieve a high precision charge measurement it is necessary to account for this effect. Cross-talk values were determined from experimental data by calculating ratios of (negative) charges in strips far away from the charge cluster to the total cluster charge. (A distance of more than four channels from the charge cluster maximum was required.)

Our final measured charge for a strip was obtained by applying this cross-talk correction from all the other adjacent strips in a cluster to the charge determined at the intermediate step ii).

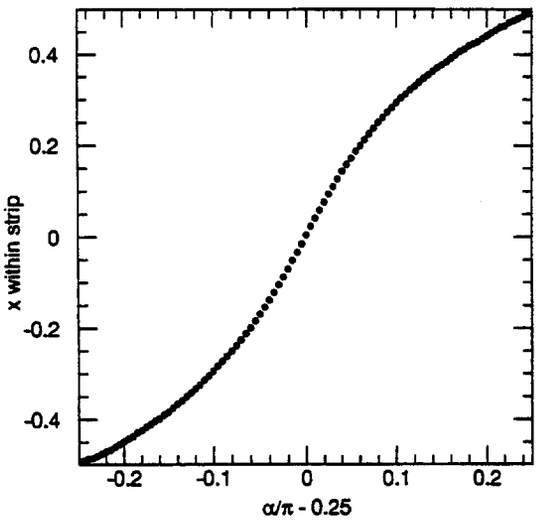

Figure 9: The measured dependence of x (within the strip) on α.

5.2 Position Determination

To determine the track or the X-ray position we used two algorithms:

- The five node center-of-gravity algorithm (c.o.g.)
- The ratio algorithm, similar to one described in [7], [9].

The ratio algorithm uses three variables – the maximum charge, $Q_{\max}$, and the charges in strips adjacent to the maximum, Q_{left} and Q_{right}. For each measurement the variable

$$\alpha = \arctan(Q_{\max} - Q_{\text{left}})/(Q_{\max} - Q_{\text{right}})$$

was calculated. There is a unique $x - \alpha$ relationship, shown in Figure 9. We use the c.o.g. algorithm to determine the x value for each bin in α. Since there are only three nodes involved in the ratio method one can expect less noise contribution to the position resolution than in a five strip c.o.g. method. But, according to our Monte Carlo studies, the ratio algorithm is more sensitive to calibration uncertainties and for large gas amplification values both methods provide practically the same resolution (Fig. 10).

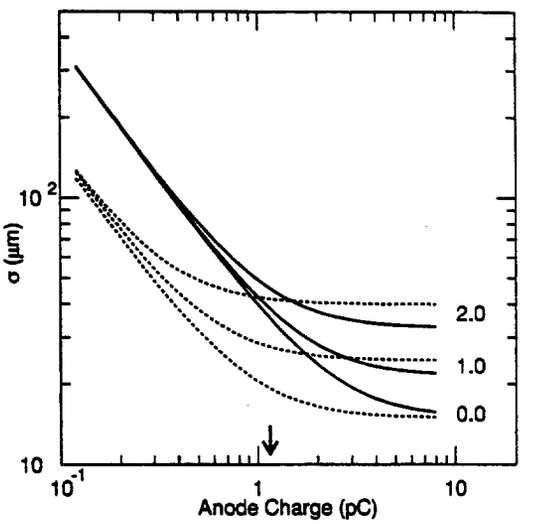

Figure 10: Position resolution dependence on the total anode charge, calculated by Monte Carlo method. Solid line is for the center of gravity algorithm, dashed line is for the ratio method. Numbers at curves correspond to the calibration uncertainty in percent. An arrow shows the anode charge of 1.15 pC – our operating point in most of the runs described in the text.

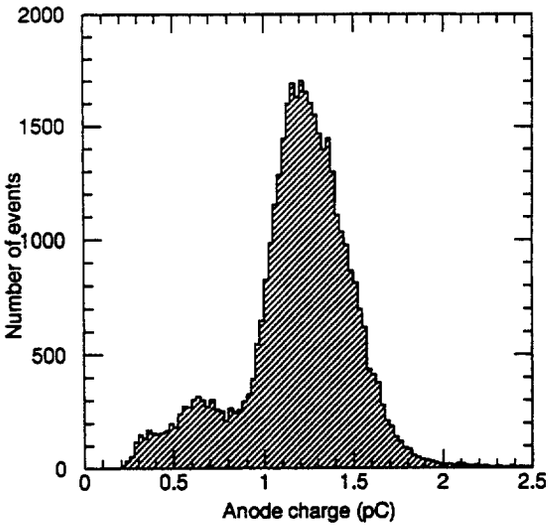

Figure 11: The amplitude spectrum of a ^{55}Fe source (measured with the gas mixture of 30%Ar+50%CO_2+20%CF_4).

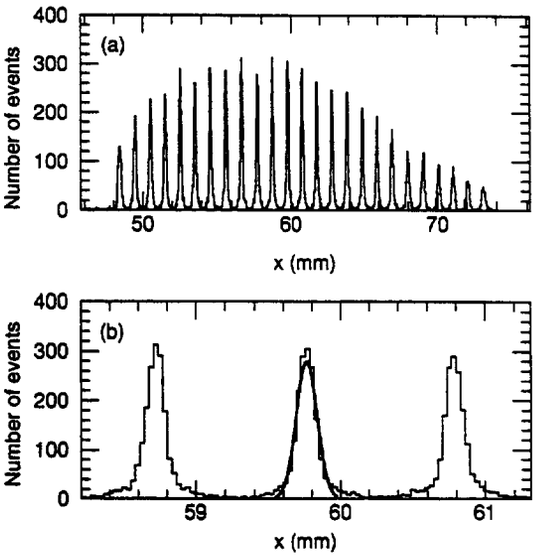

Figure 12: (a) Reconstructed X-ray absorption location representing the collimator's slit image. (b) Three of the peaks magnified.

6 Results

6.1 ^{55}Fe Measurements

Figure 11 shows the pulse height spectrum obtained with a ^{55}Fe source. The spectrum width is affected by two factors. First, the charge is measured on one cathode plane only and the induced charge distribution depends on whether the X-ray is absorbed between the anode and readout cathode strip or between the anode and the non-segmented cathode [8]. Second, the presence of CF_4 in the gas mixture results in capture of drift electrons, especially in the high field around the anode wires [25], [26].

Figure 12 presents the X-ray position spectrum. The multiple peaks in the position spectrum are caused by the collimator shown in Fig. 8b. A Gaussian fit was used to determine each peak position and width. A 1% parallax correction due to the geometrical divergence (Fig. 8b) was taken into account in the analysis. The collimator slit pitch is known with high precision, which enables us to relate measured peak positions to true positions.

Figure 13 compares measured and expected charge collected on one readout strip versus the distance between the strip center and the avalanche position. The calculated dependence used the induced cathode charge distribution based on a one-parameter Gatti function [23]. The measured dependence exhibits significant tails. For the c.o.g. algorithm this results in a systematic shift in measured positions (Fig. 14a), because five strips do not contain all the charge. To determine the position correctly this nonlinearity must be taken into account (Fig. 14b).

Figure 15a shows the peak width dependence on the peak number. Beam divergence produces a geometrical spread, due to the nonzero projection of X-rays on the anode wire (Fig. 8b). Experimental data was fit with a dependence $\sigma_i = \sqrt{\sigma_0^2 + (\sigma_\varphi \cdot |i - i_c|)^2}$, where σ_0 is the peak width at the vertical incidence point i_c and $\sigma_\varphi \cdot |i - i_c|$ is the width due to beam divergence. The value of σ_0 resulting from the fit is, in turn, the result of a convolution of a 100 μm wide uniform distribution (due to the collimator slit width) with a chamber resolution function presumed to be Gaussian. Figure 15b shows the relationship between the width of the composed distribution, σ_0, and the width of the convoluting Gaussian, σ.

Figure 16 shows the dependence of the position resolution on total anode charge. For ^{55}Fe X-rays the position resolution is limited by the photoelectron range. The lines in Figure 16 show the

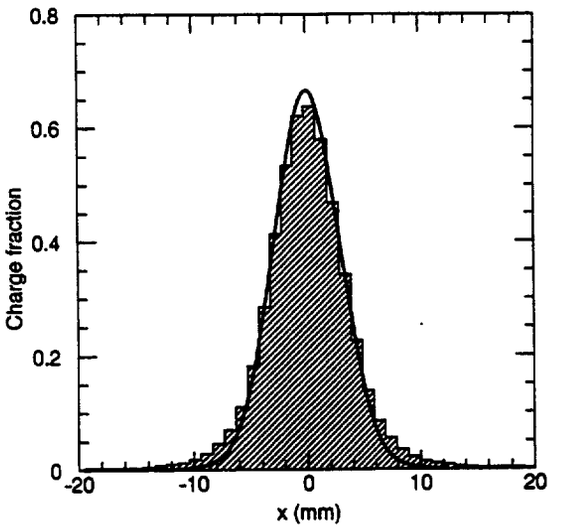

Figure 13: Comparison of measured (histogram) and calculated (line) charge collected on one readout strip versus the distance between the strip center and the avalanche position.

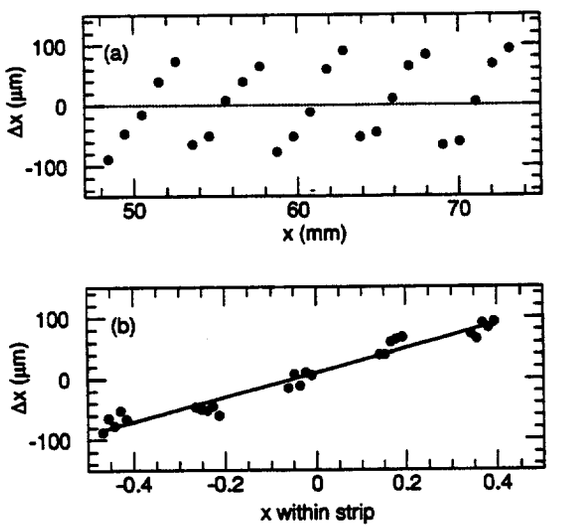

Figure 14: The difference between true and measured slit positions: (a) vs. slit position, (b) vs. the slit position within a strip. The linear fit shown in (b) was used to correct track position for nonlinearity.

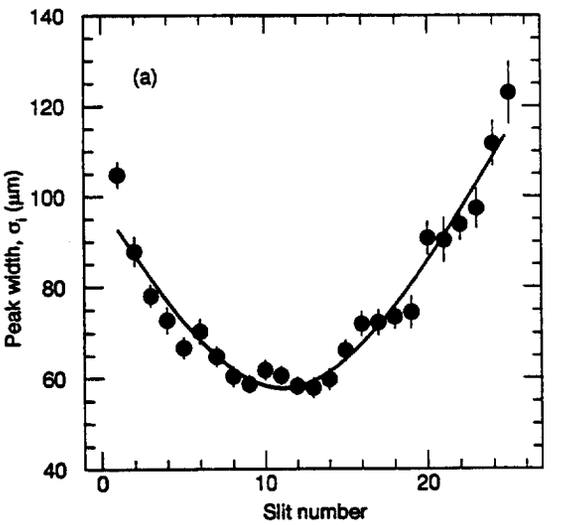

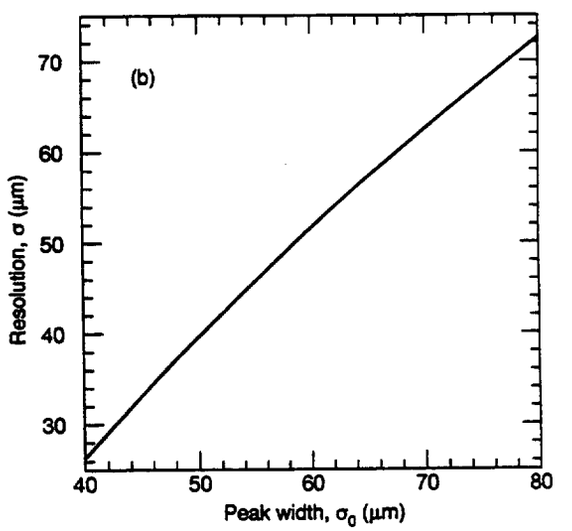

Figure 15: (a) Peak width dependence on the slit number. The fit used to determine the σ_0 value is shown by the solid line. (b) Chamber resolution, σ, as a function of the width of the observed distribution, σ_0.

resolution dependence calculated using the Monte Carlo simulations described in Section 3 with the addition of the photoelectron range effect based on data from [18]. The difference in σ values in Figure 16a and b is due to the different gas densities and, hence, the different ranges of photo- and Auger electrons. Deviation of the measured resolution from calculations is in part due to the effect of the photon assisted avalanche growth [18], which was not included in our Monte Carlo simulations.

6.2 Particle Beam Measurements

Figure 17 shows a hit distribution (beam profile), using the center of the strip with the maximum charge deposition as the hit position.

To select high energy muons the following selection criteria were applied:

- The amplitude of the signal in the scintillating counter Sgem (Fig. 8a) should be less than 200 ADC counts. (To remove shower events.)
- The FADC value in the strip with maximum count should be less than 800 counts. (To exclude the region were calibration is done by extrapolation.)
- The total charge in a 5 strip cluster should be more than 4.0 fC. (To remove empty events.)

Figure 18 shows an amplitude distribution for the selected events, demonstrating the Landau fluctuations of the deposited charge.

As we mentioned above, there is some nonlinearity inherent in the c.o.g. algorithm. This nonlinearity is clearly seen as dips at strip boundaries on the muon beam profile distribution without correction (Fig. 19a). The amount of charge on one strip for the muon data has the same dependence on the distance to the avalanche as for the X-ray data (Fig. 13). Therefore we used the same nonlinearity correction for the c.o.g. algorithm as above (Fig. 14b).

Data taken with the comb counter implemented in the trigger was used to check for any nonlinearity remaining after the above correction. There are multiple peaks observed in the muon position spectrum for dedicated comb counter runs (Fig. 20a). These data were processed in a similar way as the ^{55}Fe data (Fig. 12). Figure 20b shows the dependence of the difference between

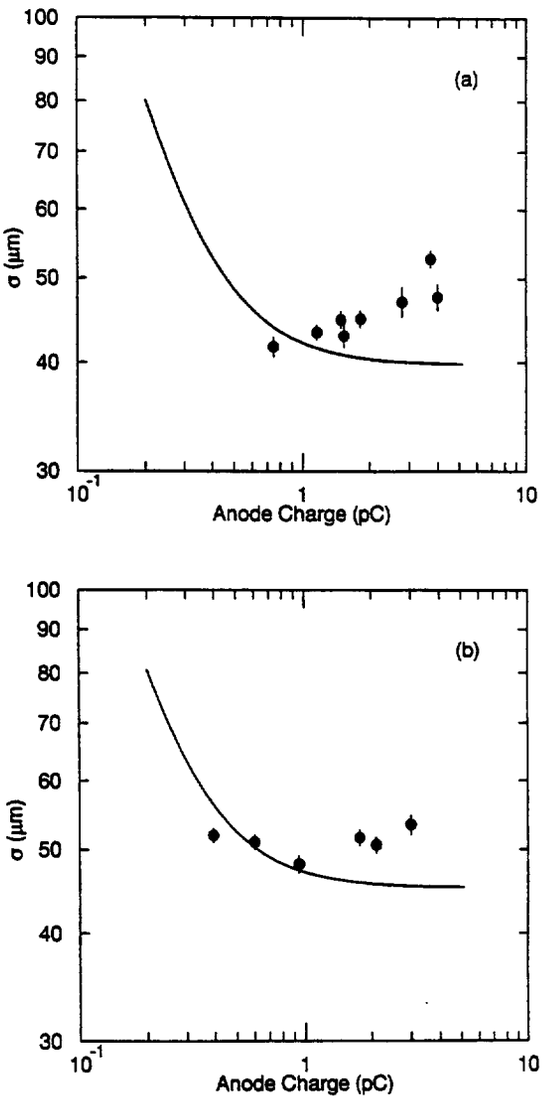

Figure 16: The position resolution determined by the ratio method as a function of total anode charge measured for ^{55}Fe X-rays. The line is from Monte Carlo simulations. (a) For a gas mixture of 30%Ar+50%CO_2+20%CF_4. (b) For a gas mixture of 80%Ar+20%CO_2.

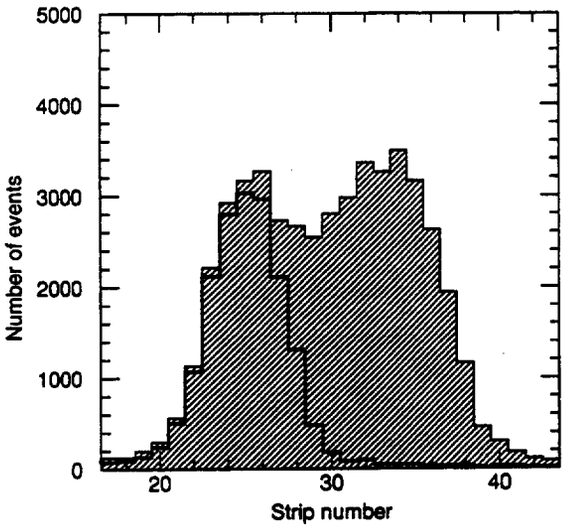

Figure 17: Hit distribution of events used to determine the global resolution. The solid line shows the beam profile for one particular run.

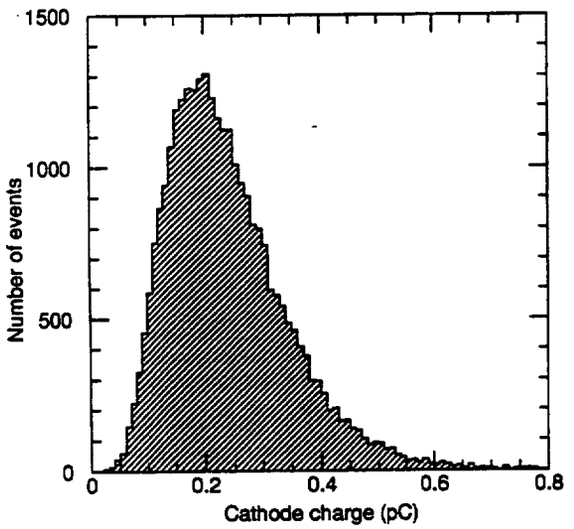

Figure 18: Charge distribution for the selected events.

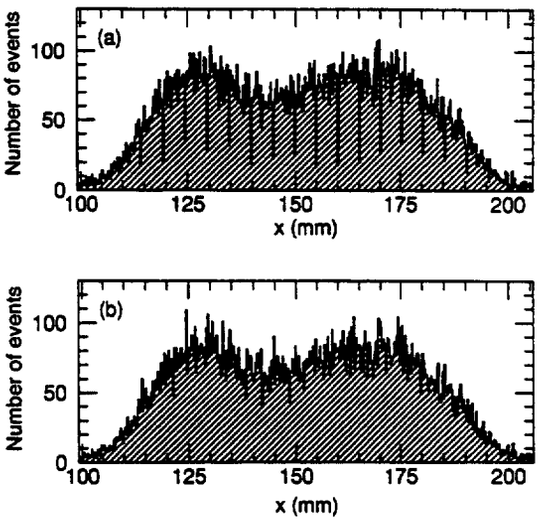

Figure 19: (a) The beam profile distribution for reconstructed tracks without correction for nonlinearity. (b) The same after corrections.

measured and true peak positions, Δx, on the peak position, x_{true}. Note the absence of a systematic nonlinearity in Figure 20c (without correction, positions are systematically shifted up to a 100 μm at the strip boundaries, as in Figure 14). Figure 20d shows the dependence of Δx on x_{true} for the ratio algorithm. Fluctuations of Δx in Figure 20d are mostly due to calibration errors.

6.2.1 Position Resolution

To determine the position resolution we used the residuals of the expected and measured track position. One of the four layers was not included in the track determination (test layer).The other three layers determined the track parameters to calculate the expected position of the track in the test layer. This procedure was applied for each layer. The width of the residual distribution is determined by the test layer resolution and by the uncertainty in the expected track position added in quadrature. The error in the expected track position was, in turn, determined by the resolution of the other three layers. To determine the chamber resolution per layer from the measured residual distributions we calculated the scale factors using the setup geometry. Assuming the same position resolution for all layers those factors are

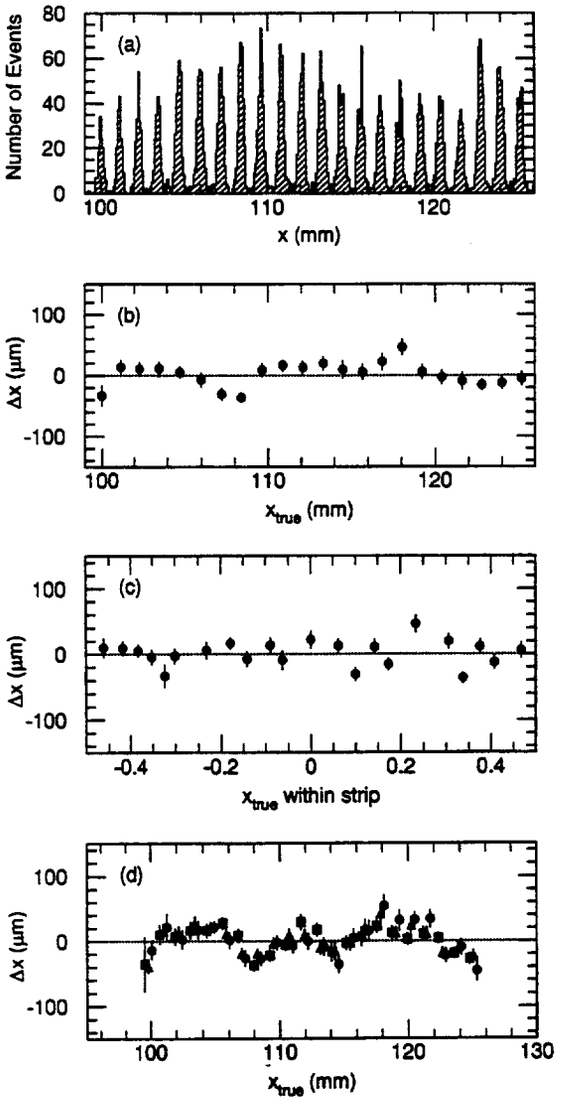

Figure 20: Analysis of muon beam data with the comb counter in trigger. (a) Beam profile for the c.o.g. algorithm after the nonlinearity correction. (b) The dependence of the difference between measured and true peak positions, Δx, on the peak position, x_{true}. (c) The same for x_{true} within a strip. (d) The dependence of Δx, on the comb counter peak position, x_{true}, for x measured by the ratio algorithm. Squares, triangles and circles correspond to different positions of the comb counter.

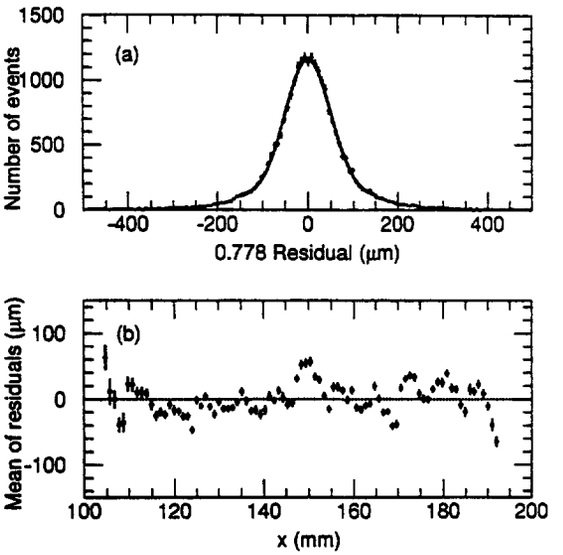

Figure 21: (a) Scaled residual distribution for normal particle incidence for a large area in layer 3. Positions were determined by the c.o.g. algorithm. Fit to a Gaussian plus a constant shown by the solid line, corresponds to $\sigma = 50.4$ μm. (b) Mean values of (non-scaled) residual distributions vs. track position in layer 3 for a c.o.g. algorithm.

0.627 for the outside layers and 0.778 for the inner layers. Figure 21a shows the scaled residual distributions for normal particle incidence. One can see non-Gaussian tails, probably related to δ-electron production. Thus to determine the width of this distribution, σ, we use two methods:

- σ was determined from a fit to a Gaussian plus a constant in a $\pm 3\sigma$ range.
- σ = FWHM/2.35.

Both methods produced the same values of σ.

Several factors affect the track position measurement: electronics noise, avalanche spread along the anode wire, calibration errors, etc. Some of these factors degrade the local resolution, others produce systematic local shifts in the measured position, thus degrading the global resolution, determined over a large chamber area. Figure 21b shows residual mean values sampled over 1/5 of the strip width ($\approx$ 1 mm) vs. track position. The spread of these mean values is a result of all charge measurement errors: calibration uncertainties, imperfect cross-talk and tails

Table 1: Local and global resolutions averaged over all four layers for a normal muon incidence and average anode charge of 1.15 pC.

Algorithm	σ_{local} (μm)	σ_{global} (μm)
Five Strip c.o.g.	41.4±1.2	50.2±0.3
Ratio Method	28.9±0.6	39.7±0.2

corrections, etc. The above uncertainties would limit the single layer resolution to $\approx 27\mu$m even with a perfect intrinsic single layer resolution and without any noise. This demonstrates the importance of the calibration procedure for a precision track position measurement. To estimate the influence of those factors, one can compare the local resolution (defined as the resolution for tracks within the same readout segment of 5 mm) and the global resolution (for a large chamber area). Table 1 compares local and global resolution (averaged over all four layers) for both algorithms for normal track incidence ($\varphi = 0, \theta = \pi/2$). As expected, the ratio algorithm provides better resolution, especially the local one. Figure 22a shows the scaled residual distribution (all four layers combined) for a normal particle incidence for a large chamber area (Fig. 19b) demonstrating $\sigma_{\text{global}} = (39.65 \pm 0.24)\mu m$. For comparison, Figure 22b shows the scaled residual distribution for the area of one strip (5.08 mm) in layer 4 where the best local resolution of $\sigma_{\text{local}} = (27.25 \pm 1.1)\mu m$ was achieved. All results presented below are based on the ratio algorithm and for a large chamber area, unless otherwise stated.

One can study the electronic noise and the intrinsic chamber contributions to the resolution by comparing resolutions at different values of deposited charge. Figure 23 shows the resolution dependence on anode charge. To measure this dependence we used runs with different values of chamber high voltage (Figure 23a). For each run the Landau spectra has been also divided into four bins, and we determine the resolution for each bin (Figure 23b). The lines in Fig. 23 correspond to the Monte Carlo calculations using the measured noise value of 2650 e and assuming 1.5% calibration uncertainty.

The angular dependence of the resolution was studied by rotating the chamber with respect to the beam. In our geometry (Fig. 8) the resolution

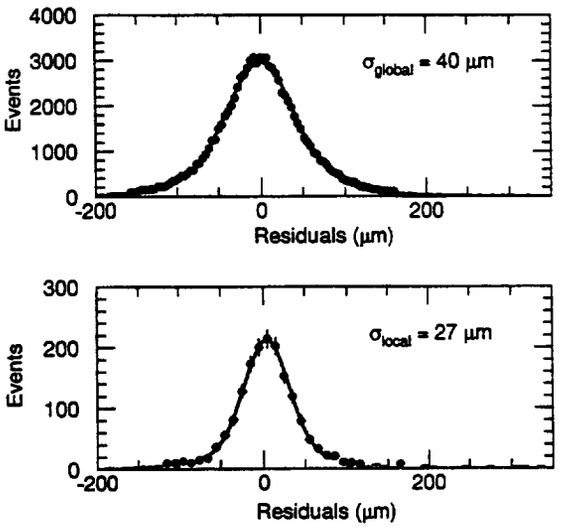

Figure 22: Local and global resolutions determined by ratio method for a normal particle incidence and average anode charge of 1.15 pC. (a) Scaled residual distribution (all four layers combined) for a large chamber area. (b) The best local resolution was achieved in layer 4.

is more affected by the φ angle, since this angle determines the track projection on the anode wire. Besides this factor, the resolution is degraded by fluctuations in the initial ionization cluster density on the track, by fluctuations in the number of secondary electrons in clusters, and by the electron multiplication near the anode. The angular dependence is important because it often dictates the chamber segmentation in φ for collider experiments. Figure 24 presents the resolution dependence on the angle φ and the Monte Carlo calculations.

The resolution dependence on φ can be written as

$$\sigma = \sqrt{\sigma_0^2 + (\sigma_\varphi \cdot \tan\varphi)^2},$$

where σ_0 is the resolution for tracks with $\varphi = 0$ and σ_φ is the contribution to the resolution due to a non-zero track projection on the anode. Our data provide $\sigma_\varphi = 0.66$ mm, which is not in good agreement with $\sigma_\varphi = 0.53$ mm from the Monte Carlo calculations shown by the solid line in Figure 24. Note that this Monte Carlo value agrees well with the value $\sigma_\varphi = 0.50$ mm derived from the data of [9] that were rescaled to match our

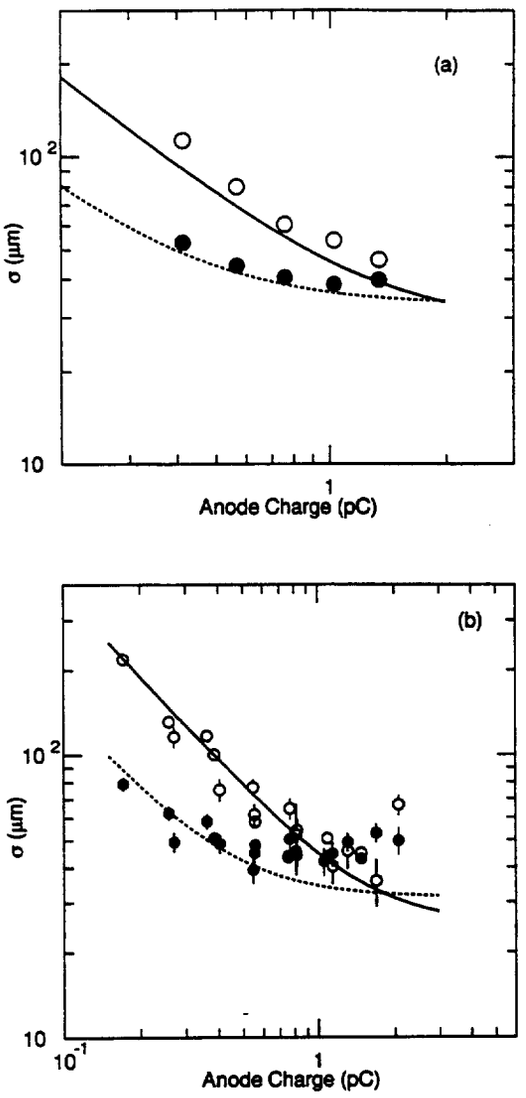

Figure 23: Charge dependence of the resolution for a normal track incidence. For the center of gravity algorithm: data – open circles, solid line – Monte Carlo calculations. For ratio method: data – solid points, dashed line – Monte Carlo. (a) Resolution for the whole Landau spectrum. (b) Resolution determined for separate bins of the Landau spectrum.

smaller anode gap.

As one can see, our measured σ_φ is larger than the corresponding Monte Carlo value. This is probably due to an electron capture process in CF_4 that is not included in the Monte Carlo. According to [25], [26], this gas exhibits a strong electron capture property in a high electric field near the anode wire. Because of this process, part of the initial clusters may disappear, thus increasing the ionization density fluctuations. In order to estimate the effect of electron capture, we compare the relative widths of the ^{55}Fe amplitude spectra, $\delta = \frac{FWHM}{2.35<Q>}$, measured in gas mixtures with and without CF_4. The relative width, δ, is the result of the fluctuations of the number of electrons, $\delta_e = 1/\sqrt{N_e}$, and the chamber resolution itself, δ_{ch}, added in quadrature: $\delta^2 = \delta_e^2 + \delta_{ch}^2$. Thus, for the two gas mixtures, with and without CF_4,

$$\delta^2_{CF_4} - \delta^2_{noCF_4} = \frac{1}{\beta N_e} - \frac{1}{N_e},$$

where β is the probability that a primary electron is not captured. Using the measured values of $\delta_{CF_4} = 0.16$ (for the 30%Ar+50%CO_2+20%CF_4 gas mixture, Figure 16) and $\delta_{noCF_4} = 0.12$ (for the gas mixture of 80%Ar+20%CO_2) we get

$$\beta = \frac{1}{N_e(\delta^2_{CF_4} - \delta^2_{noCF_4}) + 1} \approx 0.3,$$

where $N_e \approx 200$ is the total number of the ionization electrons produced in the ^{55}Fe X-ray absorption. This estimate agrees well with the value of $\beta_{MC} = 0.31$, which makes our Monte Carlo fit the data (dashed line in Figure 24). After taking this electron capture into account, the Monte Carlo provides $\sigma_\varphi = 0.66$ mm, as expected.

Our data on φ dependence also agree with the phenomenological parameterization developed in [27], which relates the width of the Landau distribution with the position resolution for the inclined tracks:

$$\sigma_\varphi = \frac{2h}{\sqrt{12}} \cdot \frac{\sigma_L}{<Q_L>}.$$

Here h is the anode-cathode spacing, σ_L and $<Q_L>$ are the r.m.s. and the mean charge of the Landau distribution. Our observed value of $\sigma_L/<Q_L> = 0.44$ provides $\sigma_\varphi = 0.64$ mm.

The position resolution is less sensitive to the θ angle. It improves with increasing θ because of the increased track length, as can be seen in Figure 25.

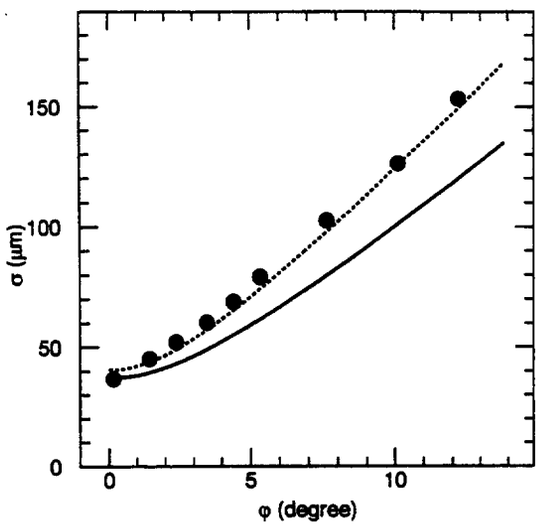

Figure 24: The resolution dependence on φ angle. Solid line shows Monte Carlo calculations without account of the electron capture process in CF_4. Dashed line shows Monte Carlo calculations using $\beta_{MC} = 0.31$ for the probability that a primary electron is not captured.

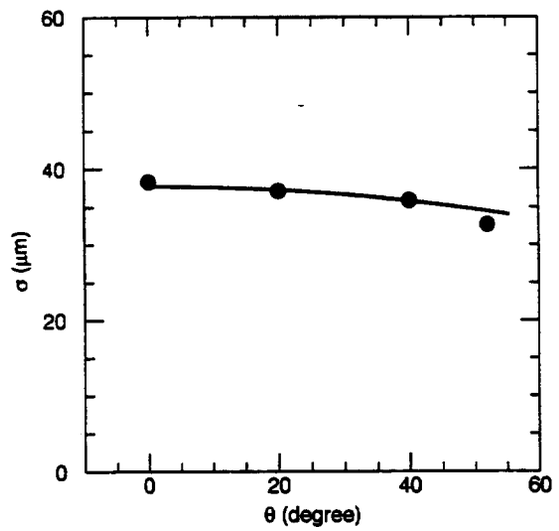

Figure 25: The resolution dependence on θ angle. Monte Carlo calculation is shown by the solid line.

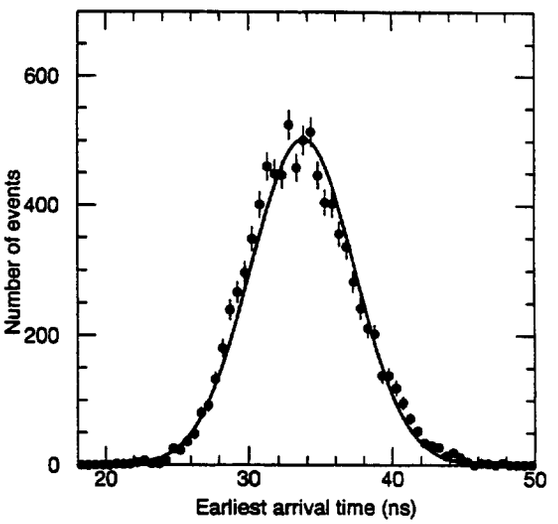

Figure 26: The software OR of all four layers. The distribution has an r.m.s. deviation of 3.6 ns.

The strip width dependence of the resolution was studied using the approximately 1/3 of chamber area implemented with wider 7 mm pitch strips. For an anode charge of 1.2 pC, the resolution of $\sigma = 64.3 \pm 0.5\mu$m was measured by the c.o.g. algorithm in the chamber area with a 7 mm pitch strips. The resolution calculated from Monte Carlo is 66.0 μm.

6.2.2 Time Resolution

The time of the fast OR output from each layer was used to study the trigger timing precision of the chambers. The discriminators used were level triggered and so were susceptible to pulse-height slewing. This was corrected offline by applying a correction factor to each fast OR based on a third order polynomial fit to the experimental distribution of the fast OR versus total charge in the layer. The stop time for the TDCs was based on the RD5 trigger pulse which had a jitter of less than 1 ns. The time of arrival of the earliest signal of all four layers is shown in Figure 26. The distribution has an r.m.s. deviation of 3.6 ns; thus, this trigger technique can easily tag the bunch crossing at collider experiments even with just a four layer superlayer.

One concern of using the earliest signal as the bunch cross tag is the susceptibility of this method

to random photon or neutron hits spoiling the time measurement. The robustness of the trigger can be improved by forming a coincidence between the earliest arrival time, T_1, and the second arrival time, T_2. The distribution of $T_2 - T_1$ from our beam test has more than 99% of the events within 12 ns.

7 Conclusion

Beam test results demonstrated the excellent position resolution of the cathode strip chambers with two intermediate strips between readout nodes. For normal track incidence, the resolution is better than 40 μm for the 5 mm readout strip pitch. This is in agreement with our Monte Carlo simulations for given gas amplification and noise level. The major factors limiting the resolution (for normal incidence) are the calibration and cross-talk correction uncertainties. Thus one can expect improvement in the position resolution with improved readout electronics and calibration procedures.

For inclined tracks the CSCs resolution is mostly determined by the track projection on the anode wire. This factor would determine the number of sectors in a muon detection system for collider experiments by limiting the maximum angle of incidence for each chamber.

The advantage of the CSC technology is the flexibility in choosing the cathode pattern. This provides an elegant way to utilize the symmetry relevant to the experiment — the cost of lithographically produced cathodes would be practically the same for linear, projective, circular or other strip patterns.

Another CSC technology advantage is the good time resolution. This provides the possibility of CSC use for the trigger and to tag the bunch crossing in collider experiments.

An important question is the CSCs performance in a magnetic field. Lorentz angle drift can degrade resolution. We used a high CO_2 content in our gas mixture to reduce the Lorentz angle effect. We have recently tested CSC performance in a magnetic field and are planning to publish results in the near future.

8 Acknowledgments

We would like to thank all our collaborators on RD5, in particular, Gyorgy Bencze for logistical help and Fritz Szoncso and Claudia E.-Wulz for setting up the DAQ system.

We also wish to thank all our collaborators on GEM for their interest, discussions and support, in particular, Igor Golutvin, Anatoly Gordeev, Kwong Lau, Gena Mitselmakher, Pavel Rehak, Alexei Vorobiev, Bill Willis and Aki Yamashita.

We are indebted to Enrico Chesi for providing us with the AMPLEX readout system he developed [28] and which was used as a basis for the design of the system used in this work.

We are grateful to Ronald Angona, Patrick Borello, August Hoffmann and Mordechai Montag for their help with engineering and manufacturing the prototype.

The authors also acknowledge the support of the following funding agencies:

- Texas National Research Laboratory Commission - award numbers RGFY92-118, RGFY93-312A, and RGFY93-304.

- US Department of Energy - contract numbers DE-AC02-76CH00016, DE-FG05-91ER40617, DE-FG02-92ER40697, and DE-FG02-91ER40676.

References

[1] G. Charpak, D. Rahm and H. Steiner, Nucl. Instr. and Meth. 80 (1970) 13.

[2] G. Charpak and F. Sauli, Nucl. Instr. and Meth. 113 (1973) 381.

[3] A. Breskin et al., Nucl. Instr. and Meth. 143 (1977) 29.

[4] G. Charpak et al., Nucl. Instr. and Meth. 148 (1978) 471.

[5] I. Endo et al., Nucl. Instr. and Meth. 188 (1981) 51.

[6] F. Piuz, R. Rosen and J. Timmermans, Nucl. Instr. and Meth. 196 (1982) 451.

[7] J. Chiba et al., Nucl. Instr. and Meth. 206 (1983) 451.

[8] J.S. Gordon and E. Mathieson, Nucl. Instr. and Meth. 227 (1984) 267.

[9] H. van der Graaf et al., Nucl. Instr. and Meth. A 307 (1991) 220.

[10] J. Fischer et al., IEEE Trans. Nucl. Sci. 37 (1990) 82.

[11] E. Beuville et al., Nucl. Instr. and Meth. A 288 (1990) 157.

[12] GEM Technical Design Report, SSCL-SR-1219, 1993.

[13] E. Gatti et al., Nucl. Instr. and Meth. 163 (1979) 83.

[14] G.C. Smith, J. Fisher and V. Radeka, IEEE Trans. Nucl. Sci. 35 (1988) 409.

[15] E. Mathieson and G.C. Smith, IEEE Trans. Nucl. Sci. 36 (1989) 305.

[16] B. Yu, G.C. Smith and V. Radeka, "Developments in interpolating cathode structures for high precision gas proportional detectors", in preparation.

[17] O. Kiselev et al., Preprint PNPI-1899, 1993 (Submitted to Nucl. Instr. and Meth.).

[18] J. Fischer, V. Radeka and G.C. Smith, Nucl. Instr. and Meth. A 252 (1986) 239.

[19] J. Sondericker III et al., Internal Note GEM TN-93-436, 1993.

[20] V.C. Ermilova, L.P. Kotenko and G.I. Merzon, Nucl. Instr. and Meth. 145 (1977) 555.

[21] G.D. Alkhazow, Nucl. Instr. and Meth. 89 (1970) 155.

[22] R. Gold and E.F. Bettnet, Phys. Rev. 147 (1966) 201.

[23] E. Mathieson and J.S. Gordon, Nucl. Instr. and Meth. 227 (1984) 277; E. Mathieson Nucl. Instr. and Meth. A 270 (1988) 602.

[24] H. Faissner et al., Status Report of the RD5 Experiment, CERN-DRDC-93-49, 1994.

[25] L.G. Christophorou et al., Nucl. Instr. and Meth. 163 (1979) 141.

[26] B.A. Dolgoshein et al., Nucl. Instr. and Meth. A 294 (1990) 473.

[27] P. Rehak and E. Gatti, "Semiconductor Detectors in Nuclear and Particle Physics", submitted to Proceedings of the 5th Conference on the Intersections of Particle and Nuclear Physics, 1994, St. Petersburg, Florida.

[28] E. Chesi et al., Nucl. Instr. Meth. A 283 (1989) 602